INTERNATIONAL JOURNAL FOR NUMERICAL METHODS IN FLUIDS, VOL. 15, 127–146 (1992)

A SIMPLE NUMERICAL TECHNIQUE FOR TURBULENT FLOWS WITH FREE SURFACES

C. M. LEMOS*

Department of Hydraulic, Maritime and Environmental Engineering, Catalonia University of Technology, Calle Gran Capitán, s/n, 08034 Barcelona, Spain

SUMMARY

A simple technique is presented for the numerical solution of two-dimensional time-dependent flows, either laminar or turbulent, involving multiple free surfaces of arbitrary configuration. The governing equations are the Reynolds equations for incompressible fluids with Boussinesq closure, the k- and ε-equations and an additional equation describing the fluid configuration. This technique can potentially describe the propagation, deformation and overturning of pre-breaking waves and the mean flow, surface configuration and turbulence field after breaking. The properties of the method are illustrated by several calculational examples. The main parts of the algorithm are optimized for vector processing in a form suitable for installation in supercomputer facilities.

KEY WORDS Turbulence Free surface k–ε model Numerical Algorithm

1. INTRODUCTION

In recent years numerical modelling has been successfully applied to many difficult free surface flow problems such as propagation, reflection and interaction of highly non-linear waves, wave overturning, waves breaking over submerged obstacles, ship waves and dam-break problems. The occurrence of the breaking phenomenon introduces abrupt and complicated changes in the behaviour of the flow, whose mathematical description is difficult. Non-breaking wave motion is nearly irrotational. Consequently, several theoretical models are available to predict the evolution of the flow.[1] However, after breaking, intense vorticity, turbulence and energy dissipation are generated. In this stage the complexity of the turbulence transport processes precludes the application of the theoretical models used for treating pre-breaking and overturning motion.[2]

In this work a new algorithm for studying two-dimensional time-dependent flows with arbitrary free surface configuration is described. The governing equations are the Reynolds equations for the mean velocity and pressure with Boussinesq (eddy viscosity) closure, the modelled k- and ε-equations[3,4] and an additional equation which defines the fluid configuration by means of the volume-of-fluid (VOF) F-function.[5] The solution algorithm, from hereon called 2D-HYDROTUR, has been developed by the author as an extension of the SOLA-VOF[6] programme for laminar flows. The momentum and turbulence equations are discretized by means of finite differences using a combination of upstream and central differencing together with local truncation error correction terms.[7] The continuity equation is satisfied using the pressure–

* Present address: Department of Coastal and Estuarine Dynamics, Instituto Hidrografico, Rua das Trinas 49, 1296 Lisbon Codex, Portugal.

0271–2091/92/140127–20$15.00

Received May 1991
Revised October 1991

velocity iteration technique[6,8] and the F-advection equation is integrated using the donor–acceptor flux approximation.[5,6] Special attention is given to the initial and boundary conditions for the turbulence equations.

The most important feature of 2D-HYDROTUR is its capability of treating both breaking and non-breaking flows with arbitrary time-dependent configurations. This model provides an alternative tool for a self-contained study of wave transformation phenomena, including propagation, deformation, interaction and overturning of pre-breaking waves, and also the mean velocity, pressure, surface configuration and turbulence field in broken waves. This flexibility is illustrated in several calculations reported below.

Computational efficiency and reliability are important elements of the 2D-HYDROTUR programme. The most time-consuming parts of the algorithm have been programmed so as to take advantage of vector and parallel processors. The programme has been run on a large number of computers ranging from PC-compatible to large vector mainframes.

2. GOVERNING EQUATIONS

The governing equations for the mean motion of an incompressible fluid of uniform density are

$$\frac{\partial u}{\partial t}+u\frac{\partial u}{\partial x}+v\frac{\partial u}{\partial y}=-\frac{\partial \phi}{\partial x}+g_x+(\nu+itl10*\nu_t)\nabla^2 u, \tag{1}$$

$$\frac{\partial v}{\partial t}+u\frac{\partial v}{\partial x}+v\frac{\partial v}{\partial y}=-\frac{\partial \phi}{\partial y}+g_y+(\nu+itl10*\nu_t)\nabla^2 v, \tag{2}$$

$$\frac{\partial u}{\partial x}+\frac{\partial v}{\partial y}=0, \tag{3}$$

where u and v are the mean velocity components in the co-ordinate directions x and y respectively, ϕ is the mean pressure divided by the constant density (energy per unit mass due to the pressure field), g_x and g_y are the components of the body force vector in the co-ordinate directions x and y respectively, ν is the fluid kinematic molecular viscosity, ν_t is the eddy viscosity and $itl10$ is an indicator whose value is zero for a laminar flow and unity for a turbulent flow. The local state of turbulence is represented by the two equations[3]

$$\frac{\partial k}{\partial t}+u\frac{\partial k}{\partial x}+v\frac{\partial k}{\partial y}=\nabla\cdot\left[\left(\nu+\frac{\nu_t}{\sigma_k}\right)\nabla k\right]+prod-\varepsilon, \tag{4}$$

$$\frac{\partial \varepsilon}{\partial t}+u\frac{\partial \varepsilon}{\partial x}+v\frac{\partial \varepsilon}{\partial y}=\nabla\cdot\left[\left(\nu+\frac{\nu_t}{\sigma_\varepsilon}\right)\nabla \varepsilon\right]+C_1\frac{\varepsilon}{k}prod-C_2\frac{\varepsilon^2}{k}, \tag{5}$$

where k is the turbulent kinetic energy per unit mass, ε is the rate of dissipation of k, $prod$ is the production of turbulent kinetic energy,

$$prod=\nu_t\left[2\left(\frac{\partial u}{\partial x}\right)^2+2\left(\frac{\partial v}{\partial y}\right)^2+\left(\frac{\partial u}{\partial y}+\frac{\partial v}{\partial x}\right)^2\right],$$

and the eddy viscosity ν_t is defined in terms of k and ε by the expression

$$\nu_t=C_d\frac{k^2}{\varepsilon}.$$

The adopted values for the empirical constants of the k–ε model are given in Table I.

Table I. Adopted values for the empirical constants of the k–ε turbulence model (after Rodi[3])

C_d	σ_k	σ_ε	C_1	C_2
0·09	1·0	1·3	1·44	1·92

Equations (4) and (5) are derived from the exact transport equations for k and ε using closure assumptions to express the unknown correlations in terms of knowable quantities. These closure assumptions are valid only for high-intensity and nearly isotropic turbulence. In turbulent free surface flows the transition between zones with strong turbulence and zones where the flow is nearly laminar is often abrupt and intermittent. Therefore it is necessary to refine the standard k–ε model to describe such transitions properly. This problem has been analysed by several authors (see e.g. References 9–11). Following the proposal of Harlow and Nakayama,[10,11] the eddy viscosity ν_t is replaced by

$$\nu_t \frac{1-\exp(-\beta\nu/\nu_t)}{\beta\nu/\nu_t},$$

i.e. the effective eddy viscosity is reduced for low-intensity turbulence. The form of the damping function is obtained by relating the mean viscous retarding acceleration of a turbulence eddy to the Oseen approximation for the force on a sphere.[10-12] The cut-off is determined by the local turbulence Reynolds number ν_t/ν and the empirical constant β, whose recommended value is 100.

The fluid configuration is defined by a volume-of-fluid (VOF) function $F(x, y, t)$, whose value is unity at any point occupied by the fluid and zero elsewhere. Cells with $F=1$ are full of fluid whereas cells with $F=0$ are empty. Cells with F-values between zero and unity and having at least one empty neighbour contain a free surface. The equation governing the time evolution of F is

$$\frac{\partial F}{\partial t}+u\frac{\partial F}{\partial x}+v\frac{\partial F}{\partial y}=0, \tag{6}$$

which states that F moves with the fluid.

Equations (1)–(6) describe laminar or tuubulent flows with or without free surfaces. If a laminar flow is to be treated, then $itl10=0$ and the k–ε equations need not be included in the calculation. In this case (u, v) and ϕ should be interpreted as instantaneous velocity and pressure rather than as mean (ensemble averaged) quantities. Confined flows can be treated by imposing $F=1$ everywhere as the initial condition and assuring that F does not change inside the domain by correct application of the boundary conditions during the calculation.

3. FINITE DIFFERENCE FORMULATION

The governing equations are discretized using a finite difference staggered grid system of rectangular cells of variable width Δx_i and height Δy_j (Figure 1). The fictitious cells surrounding the domain are used to set boundary conditions. The arrangement of the dependent variables in a typical cell is illustrated in Figure 2.

The basic computational cycle of 2D-HYDROTUR is the following. First, explicit approximations of equations (1) and (2) are used to compute the first guess for the new time level velocities using the previous time level values of the advective, pressure, viscous and Reynolds stress

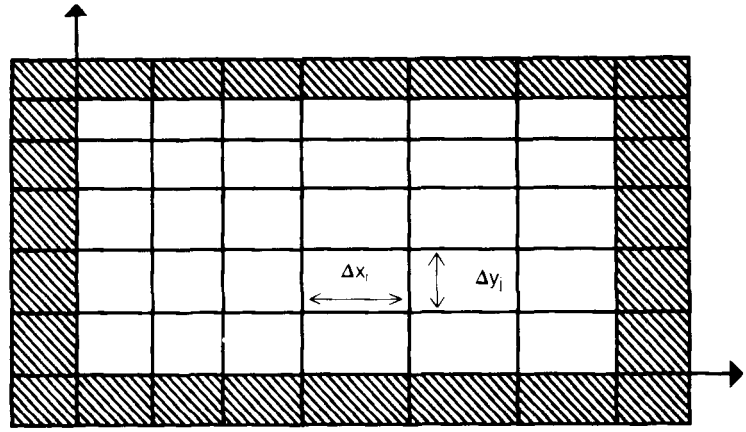

Figure 1. Finite difference mesh with variable rectangular cells

accelerations. This temporary velocity field will not in general satisfy the continuity equation (though it already carries the correct vorticity). To satisfy equation (3), pressures are iteratively adjusted in each cell in such a way that the discrete divergence in the cell is driven to zero. Then the velocity changes induced by each pressure correction are added to the temporary velocity field. After this stage equations (4) and (5) are used to update k and ε, which in turn define the time-advanced eddy viscosity. Finally the new fluid configuration is found using equation (6). The structure of the 2D-HYDROTUR algorithm is illustrated in Figure 3.

To simplify the writing of the finite difference equations in the staggered mesh, it is convenient to introduce the operators

$$\Delta_x^+ f_{i,j}=(f_{i+1,j}-f_{i,j})/\Delta x^+, \qquad \Delta_x^- f_{i,j}=(f_{i,j}-f_{i,j-1})/\Delta x^-,$$

$$\Delta_y^+ f_{i,j}=(f_{i,j+1}-f_{i,j})/\Delta y^+, \qquad \Delta_x^- f_{i,j}=(f_{i,j}-f_{i,j-1})/\Delta y^-,$$

$$\Delta_x^1 f_{i,j}=(f_{i+1/2,j}-f_{i-1/2,j})/\Delta x_i, \qquad \Delta_y^1 f_{i,j}=(f_{i,j+1/2}-f_{i,j-1/2})/\Delta y_j,$$

$$\Delta_x^0 f_{i,j}=[\Delta x^- *(\Delta_x^+ f_{i,j})+\Delta x^+ *(\Delta_x^- f_{i,j})]/(\Delta x^+ +\Delta x^-),$$

$$\Delta_y^0 f_{i,j}=[\Delta y^- *(\Delta_y^+ f_{i,j})+\Delta y^+ *(\Delta_y^- f_{i,j})]/(\Delta y^+ +\Delta y^{-1}),$$

$$\Delta_{xx} f_{i,j}=2*(\Delta_x^+ f_{i,j}-\Delta_x^- f_{i,j})/(\Delta x^+ +\Delta x^-),$$

$$\Delta_{yy} f_{i,j}=2*(\Delta_y^+ f_{i,j}-\Delta_y^- f_{i,j})/(\Delta y^+ +\Delta y^-),$$

where f is a generic variable, $\Delta x^+ = x_{i+1}-x_i$, $\Delta x^- = x_i - x_{i-1}$, $\Delta y^+ = y_{j+1}-y_j$, $\Delta y^- = y_j - y_{j-1}$ and (x_i, y_j) defines the position where $f_{i,j}$ is stored in the discrete mesh. A finite difference approximation of the momentum equations is

$$\tilde{u}_{i+1/2,j}=u^n_{i+1/2,j}+\Delta t[(\phi^n_{i,j}-\phi^n_{i+1,j})/\Delta x_i - fux^n_{i+1/2,j} - fuy^n_{i+1/2,j} + visx^n_{i+1/2,j} + itl10*reynx^n_{i+1/2,j} + g_x], \tag{7}$$

$$\tilde{v}_{i,j+1/2}=v^n_{i,j+1/2}+\Delta t[(\phi^n_{i,j}-\phi^n_{i,j+1})/\Delta y_j - fvx^n_{i,j+1/2} - fvy^n_{i,j+1/2} + visy^n_{i,j+1/2} + itl10*reyny^n_{i,j+1/2} + g_y], \tag{8}$$

where $\tilde{u}_{i+1/2,j}$ and $\tilde{v}_{i,j+1/2}$ are temporary velocities and the superscript n indicates that the terms

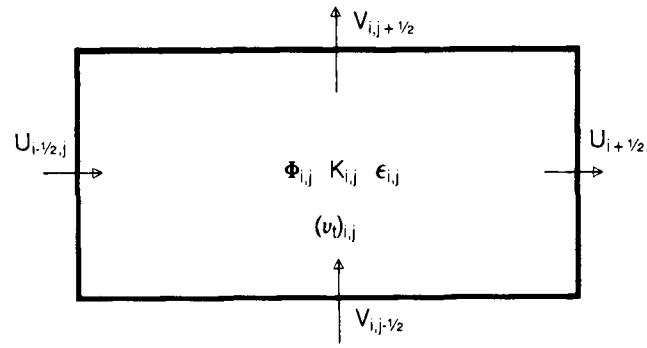

Figure 2. Location of variables in a typical mesh cell

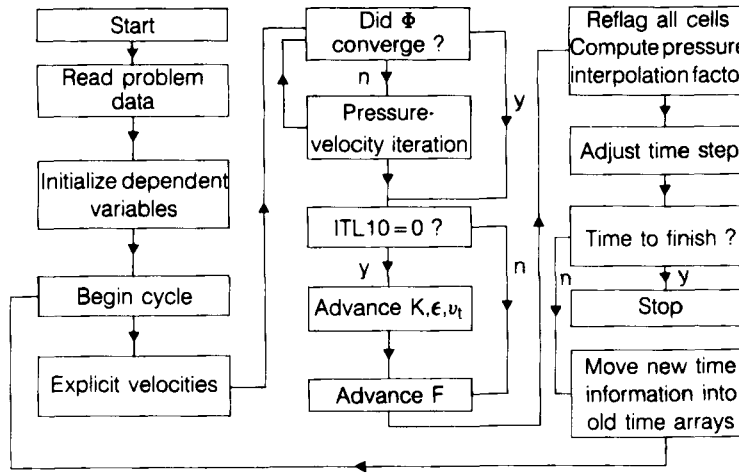

Figure 3. Structure of the 2D-HYDROTUR algorithm

are evaluated at time t. The advective, viscous and Reynolds stress acceleration terms have an obvious meaning, e.g. *fux* is the advective flux of u in the x-direction, *visx* is the x-component of the viscous acceleration and *reynx* is the Reynolds stress acceleration in the x-direction. The approximations for the advective fluxes are weighted combinations of upstream and central differencing with a parameter α that controls the relative amount of each one. The approximations for these fluxes in a variable mesh can be found in Reference 6. The centred approximations are underdiffusive and require some viscosity to remain stable. Upstream differencing has better stability properties but the resulting numerical diffusion may introduce gross errors in the computed solution. An alternative combining the advantages of both types of approximation is the introduction of local 'balancing terms' that correct the most destructive part of the truncation error.[7,13] This idea leads to the following discretization of the viscous acceleration terms:

$$visx = [\nu + (1-\alpha)(\Delta t/2)(u^2)_{i+1/2,j}]\Delta_{xx}u_{i+1/2,j} + [\nu + (1-\alpha)(\Delta t/2)(v^2)_{i+1/2,j}]\Delta_{yy}u_{i+1/2,j}, \quad (9)$$

$$visy = [\nu + (1-\alpha)(\Delta t/2)(u^2)_{i,j+1/2}]\Delta_{xx}v_{i,j+1/2} + [\nu + (1-\alpha)(\Delta t/2)(v^2)_{i,j+1/2}]\Delta_{yy}u_{i,j+1/2}. \quad (10)$$

The expressions for the modelled Reynolds stress accelerations are

$$reynx=(\nu_t)_{i+1/2,j}(\Delta_{xx}+\Delta_{yy})u_{i+1/2,j}, \tag{11}$$

$$reyny=(\nu_t)_{i,j+1/2}(\Delta_{xx}+\Delta_{yy})v_{i,j+1/2}. \tag{12}$$

To satisfy the continuity equation, pressures and velocities are adjusted in each cell occupied by fluid.[6,8] In full cells the pressure is changed in such a way that the discrete divergence $d_{i,j}$ of the temporary velocity is driven to zero. The pressure change is

$$\Delta\phi_{i,j}=-\frac{d_{i,j}}{\partial[d_{i,j}]/\partial\phi}, \tag{13}$$

where

$$d_{i,j}=\Delta_x^1 u_{i,j}+\Delta_y^1 v_{i,j},$$

$$\frac{\partial[d_{i,j}]}{\partial\phi}=\Delta t\left[\frac{1}{\Delta x_i}\left(\frac{1}{\Delta x_{i+1/2}}+\frac{1}{\Delta x_{i-1/2}}\right)+\frac{1}{\Delta y_j}\left(\frac{1}{\Delta y_{j+1/2}}+\frac{1}{\Delta y_{j-1/2}}\right)\right].$$

The pressure and velocities in the faces of cell ij are updated as follows:

$$\phi_{i,j}^{(new)}\leftarrow\phi_{i,j}^{(old)}+\Delta\phi_{i,j},$$

$$u_{i+1/2,j}^{(new)}\leftarrow u_{i+1/2,j}^{(old)}+\Delta\phi_{i,j}*\Delta t/\Delta x_{i+1/2,j}, \qquad u_{i-1/2,j}^{(new)}\leftarrow u_{i-1/2,j}^{(old)}-\Delta\phi_{i,j}*\Delta t/\Delta x_{i-1/2,j},$$

$$v_{i,j+1/2}^{(new)}\leftarrow v_{i,j+1/2}^{(old)}+\Delta\phi_{i,j}*\Delta t/\Delta y_{i,j+1/2}, \qquad v_{i,j-1/2}^{(new)}\leftarrow v_{i,j-1/2}^{(old)}-\Delta\phi_{i,j}*\Delta t/\Delta y_{i,j-1/2},$$

where the superscripts (new) and (old) denote iteration levels. This pressure-velocity iteration technique is a special form of Newton's method applied to the (discrete) pressure Poisson equation for incompressible flow.[8,10] In cells containing a free surface the continuity equation is replaced by the dynamic condition of continuity of the normal stress, i.e. the pressure is computed in such a way that an interpolation between the surface cell pressure and the pressure in the nearest-neighbour full cell yields the correct pressure at the free surface.[8,14] One complete iteration consists of correcting the pressures and velocities in all cells occupied by the fluid. The mesh must be swept several times until convergence is reached.

After determining (u, v) and ϕ, equations (4) and (5) are advanced in time to update the turbulence field and define ν_t at the new time level. The approximations for the k- and ε-equations are

$$\varepsilon_{i,j}^{n+1}=\frac{\varepsilon_{i,j}^n/\Delta t-fepx_{i,j}^n-fepy_{i,j}^n+visep_{i,j}^n+C_1*(\varepsilon/k)_{i,j}^n*prod_{i,j}^n}{1/\Delta t+C_2(\varepsilon/k)_{i,j}^n}, \tag{14}$$

$$k_{i,j}^n=k_{i,j}^n+\Delta t\{-fkx_{i,j}^n-fky_{i,j}^n+visk_{i,j}^n+\tfrac{1}{2}[(prod-\varepsilon)^{n+1}+(prod-\varepsilon)^n]_{i,j}\}. \tag{15}$$

The advective and diffusive terms have an obvious meaning, e.g. $fkx=u(\partial k/\partial x)$. For example, the approximation for fkx is

$$fkx=\frac{u_{i,j}^{n+1}}{\Delta x_\alpha}\{\Delta x_l(\Delta_x^+ k_{i,j})+\Delta x_r(\Delta_x^- k_{i,j})+\gamma\,\mathrm{sgn}(u_{i,j}^{n+1})[\Delta x_r(\Delta_x^- k_{i,j})-\Delta x_l(\Delta_x^+ k_{i,j})]\},$$

where $\Delta x_\alpha=\Delta x_r+\Delta x_l+\mathrm{sgn}(u_{i,j}^{n+1})(\Delta x_r-\Delta x_l)$ and the space increments Δx_r and Δx_l are the distances between the centre of cell ij and the centre of its right and left neighbours respectively. The weighting factor γ controls the amount of upstream differencing for the turbulence equations

and may be chosen different from α. The diffusion terms such as *visk* are discretized as

$$visk = \Delta_x^1[(v + v_t/\sigma_k)\Delta_x^1 k]_{i,j}^n + \Delta_y^1[(v + v_t/\sigma_k)\Delta_y^1 k]_{i,j}^n + \tfrac{1}{2}(\gamma - 1)\Delta t[(u^2)_{i,j}^{n+1}\Delta_{xx}k_{i,j}^n + (v^2)_{i,j}^{n+1}\Delta_{yy}k_{i,j}^n].$$

The last step of the computational cycle consists of advancing the F-function in time using equation (6). In this work the donor–acceptor flux approximation introduced by Nichols and Hirt[5] is used. A detailed discussion of this topic can be found in References 5 and 6.

4. BOUNDARY CONDITIONS

The governing equations contain six dependent variables (u, v, ϕ, k, ε and F). Equations (1), (2), (4) and (5) are second-order parabolic in time and thus boundary conditions for (u, v), k and ε must be prescribed on every boundary point. Equation (6) is a first-order hyperbolic equation and requires one boundary condition to be specified on every boundary point where the streamlines (characteristics) enter the fluid domain. In an incompressible flow, boundary conditions for ϕ are not required. A significant advantage of the pressure–velocity relaxation technique is that artificial boundary conditions for ϕ are not required.[15]

At the regular mesh boundaries a variety of boundary conditions can be imposed using the fictitious cells around the mesh. The present algorithm incorporates free slip, no-slip, continuative, periodic, constant pressure and law-of-the-wall boundary conditions.[6] These latter are vital for calculating turbulent flows near solid walls, by providing boundary conditions for the tangential velocity, k and ε, and will therefore be discussed in some detail.

In a constant stress turbulent boundary layer the local state of turbulence is characterized in terms of the friction velocity u_*. In the 2D-HYDROTUR model u_* is calculated using a combination of the linear and logarithmic wall laws,[12,16]

$$u_* = \max[X * |u_w|, (|u_w| v/y_w)^{1/2}], \tag{16}$$

where u_w and y_w are the mean velocity and the distance from the wall for the layer of mesh cells adjacent to the boundary. X is the solution of the implicit equation

$$X \ln(A * X) - \kappa = 0, \tag{17}$$

where $A = E|u_w| y_w/v$, $\kappa \simeq 0{\cdot}41$ and $E \simeq 9{\cdot}0$. The friction velocity provides boundary conditions for the tangential velocity, k and ε in all mesh cells adjacent to the wall.[3] Referring to Figure 4, these

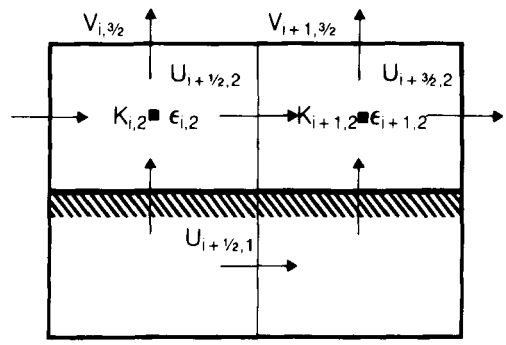

Figure 4. Schematization of wall boundary conditions in a turbulent flow

boundary conditions are

$$u_{i+1/2,1} = u_{i+1/2,2} - \mathrm{sgn}(u_{i+1/2,2}) u_* \frac{\Delta y_1 + \Delta y_2}{\kappa \Delta y_2}, \tag{18}$$

$$k_{i,2} = \frac{u_*^2}{(C_d)^{1/2}}, \tag{19}$$

$$\varepsilon_{i,2} = \frac{u_*^3}{\kappa y [1 - \exp(-u_* y / 26\nu)]}. \tag{20}$$

Equation (20) states that near the boundary the eddy viscosity follows the van Driest law.[4,12] Similar wall boundary conditions are used for the other boundaries, reversing the roles of u and v as appropriate. In 2D-HYDROTUR internal obstacles may be defined by blocking out any desired combination of cells in the mesh. Around these internal obstacles, free slip, no-slip and law-of-the-wall boundary conditions may be imposed.

In cells containing a free surface the correct boundary conditions are the continuity of the velocity and stress vectors (called the kinematic and dynamic boundary conditions respectively) plus special boundary conditions for k and ε. The kinematic boundary condition is automatically satisfied in the F-advection step. The dynamic boundary condition for the normal stress component of the stress vector is imposed during the implicit pressure evaluation (Section 3). The tangential stress condition (vanishing of the tangential component of the stress vector) is approximated by specifying velocities immediately outside the free surface where these values are needed in the finite difference equations in the surface cells.[6,14] The free surface boundary conditions for k and ε are the most difficult to specify owing to the complexity of the turbulence dynamics near the interface. The solutions that have been proposed assume that the free surface has small curvature and the boundary conditions for k and ε are obtained using modified wall laws (see e.g. Reference 3). However, in strongly turbulent breaking flows the most relevant turbulence-generating processes occur inside the water body and are driven by the internal velocity shear created by the folding of the free surface. In order to derive simple and physically coherent boundary conditions for k and ε, it is better to assume that the surface interaction between air and water is of negligible significance during the time of breaking compared with the influence of the internal processes on the values of k and ε near the surface. Therefore the assumed boundary conditions at the surface are $\partial k/\partial n = 0$ and $\partial \varepsilon/\partial n = 0$. This treatment for the turbulence variables was recently proposed by Launder[17] (though in a different context and with a different theoretical justification). To simplify the application of these boundary conditions, the orientation of the free surface is sensed in a crude way. If the slope of the free surface is less than unity, $\partial/\partial n \simeq \partial/\partial y$; otherwise $\partial/\partial n \simeq \partial/\partial x$.

5. INITIAL CONDITIONS

In order to define a well-posed problem, initial conditions for u, v, F, k and ε must be supplied. The minimum requirements for the initial velocity field are the solenoidal property and the continuity of its normal component at the boundary.[15] The initial F-function distribution is chosen so that, for the desired initial fluid configuration, $F = 1$ in full cells and the fractional volume in the surface cells defines the interface shape properly.

It is very difficult to specify initial conditions for k and ε. Ideally, these conditions for the turbulence variables should be prescribed according to experimental data, but this type of information is not always available for the flow of interest. Hence either theoretical or heuristic

methods must be used. The simplest possible solution consists of prescribing constant values for k and ε (hence for ν_t). Another alternative consists of using theoretical profiles. Nevertheless, this procedure is limited to simple flow geometries and requires a detailed knowledge about the solution itself. To (partially) overcome this problem, a general purpose method for generating initial distributions for k and ε was developed in parallel with 2D-HYDROTUR. The method consists of simplifying equations (4) and (5) in such a way that the resulting equations define a boundary value problem for the turbulence variables. These simplified equations are

$$\frac{\nu_i}{\sigma_k}\nabla^2 k + prod - \varepsilon = 0, \tag{21}$$

$$\frac{\nu_i}{\sigma_\varepsilon}\nabla^2 \varepsilon + C_1 \frac{\varepsilon}{k} prod - C_2 \frac{\varepsilon^2}{k} = 0, \tag{22}$$

where ν_i is a constant viscosity with typical values from two to three orders of magnitude higher than the molecular viscosity. Equations (21) and (22) smoothly 'expand' the boundary conditions to the interior of the solution domain. This method generated good initial conditions in several test problems, such as isotropic turbulence decay, logarithmic boundary layer flow and turbulent cavity flow.

6. APPLICATIONS

In this section several numerical calculations are reported to illustrate the capabilities of the present technique for calculating free surface turbulent flows.

The first example illustrates the development of turbulence in moving hydraulic jumps generated by pushing a horizontal uniform stream of fluid into a vertical rigid wall (Figure 5). The celerity C at which a hydraulic jump moves and the fluid height at the wall, h_1, are obtained from the mass and momentum conservation laws

$$u_2 = \left(1 - \frac{h_1}{h_2}\right) C, \qquad C = \left(g \frac{h_2}{h_1} \frac{h_1 + h_2}{2}\right)^{1/2},$$

given g, u_2 and h_2. In a frame of reference moving with the jump celerity, the flow is steady and the relevant jump properties (depth ratio h_1/h_2, surface profile, turbulent kinetic energy and shear stress distributions, etc.) might be expressed as functions of the supercritical Froude number

$$\mathbb{F} = \frac{|u_2 - C|}{(gh_2)^{1/2}}.$$

Experimental investigations on steady turbulent jumps reported in the literature (see Reference 18) usually provide information on the mean velocity and free surface configuration and on the distribution of the normal and shear turbulent stresses.

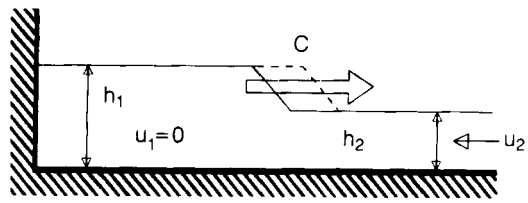

Figure 5. Schematization of the moving hydraulic jump

Figures 6 and 7 illustrate the velocity field and the distribution of k respectively for a moving jump with $\mathbb{F} = 1{\cdot}854$ and depth ratio 2·17, when the computed jump became almost stationary in a frame of reference moving to the right with velocity C. The velocity plot shows an extensive shear layer originated by the folding of the free surface, starting at the toe of the jump and ending at a distance of (aproximately) $4h_1$ downstream. Within this shear layer there was a primary recirculation region on which the turbulence intensity was maximum. Two secondary recirculation zones with non-negligible vertical velocity were found at $2h_1$ and $4h_1$ downstream of the jump's front. The occurrence of these 'roll vortices' is well documented in the literature of surf zone hydrodynamics.[2,19] Several small void regions were observed inside the body of the jump, caused by the violence of the initial breaking. In nature, significant air concentrations would be found instead. The inadequacy of the present model to represent air–water mixing (which introduces physical effects that violate the incompressibility hypothesis) has to be regarded as a significant limitation which has to be overcome in the future. The relevant turbulence dynamics was confined to the surface shear layer, the bottom-generated turbulence being irrelevant (as expected). In this surface layer, values of the eddy viscosity ranging from $1{\cdot}5 \times 10^{-2}$ to

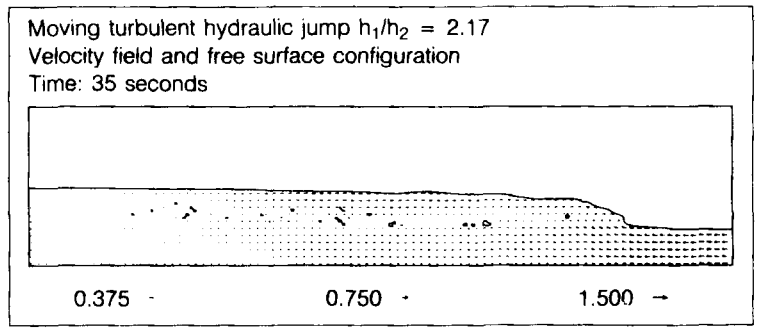

Figure 6. Computed velocity field and free surface configuration for a moving jump with $h_1/h_2 = 2{\cdot}17$

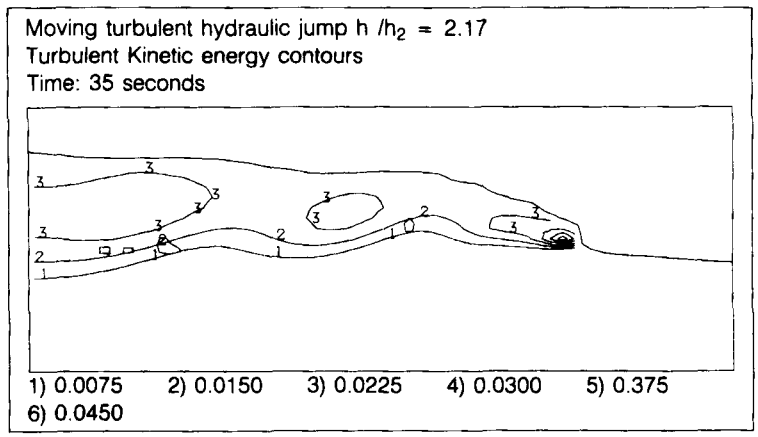

Figure 7. Computed turbulent kinetic energy for a moving jump with $h_1/h_2 = 2{\cdot}17$

$3{\cdot}0 \times 10^{-3}$ m^2 s^{-1} were found and the turbulence Reynolds number showed strong gradients. The maximum of eddy viscosity was found downstream of the main production region, showing that ε decays faster than k. There was strong production at the toe of the front, where k reached an absolute maximum of about 10% of the kinetic energy of the incident stream. Downstream of the primary production region other local maxima were found, possibly as a result of production originated by the large-scale roll vortices. The turbulence generated close to the jump front spread downwards and downstream, justifying the qualitative model of Madsen and Svendsen.[20,21] Most of the turbulence is dissipated above the height of the incident stream, i.e. at the same level where it is generated.[22] The computed h_1 at the wall was 2·20 m, with an error of 1·4% with respect to the theoretical value of 2·17. This provided an important check on momentum conservation in the present model.

Figure 8 shows a comparison between computed and experimental distributions of the dimensionless turbulent velocity fluctuations and shear stress at a distance $2{\cdot}0\ h_1$ downstream of the front of a jump with $\mathbb{F} = 2{\cdot}83$ ($h_1/h_2 = 3{\cdot}52$). This Froude number was obtained using an input stream velocity $u_2 = -2{\cdot}0$ m s^{-1} with $g = 9{\cdot}81$ m s^{-2} downwards. The computational domain was chosen 2·5 m long and 0·5 m high and was discretized using a regular mesh of 200×40 cells. The turbulent velocity fluctuations were obtained from the turbulent kinetic energy by assuming the relative strengths for a turbulent wake.[22] In general there was fair agreement except near the bottom, but some differences between the experimental and computational results should be noted. Firstly, near the bottom the computed turbulence intensity was smaller than the experimental values because bottom-generated turbulence is stronger in steady jumps than in moving jumps. Secondly, the experiments show that the relative strength of the turbulent velocity fluctuations is not constant inside the jump. This aspect of the turbulence dynamics can only be described in a numerical calculation using a more refined turbulence model. Finally, the computed downstream decay of the turbulence variables, especially of the shear stress, was

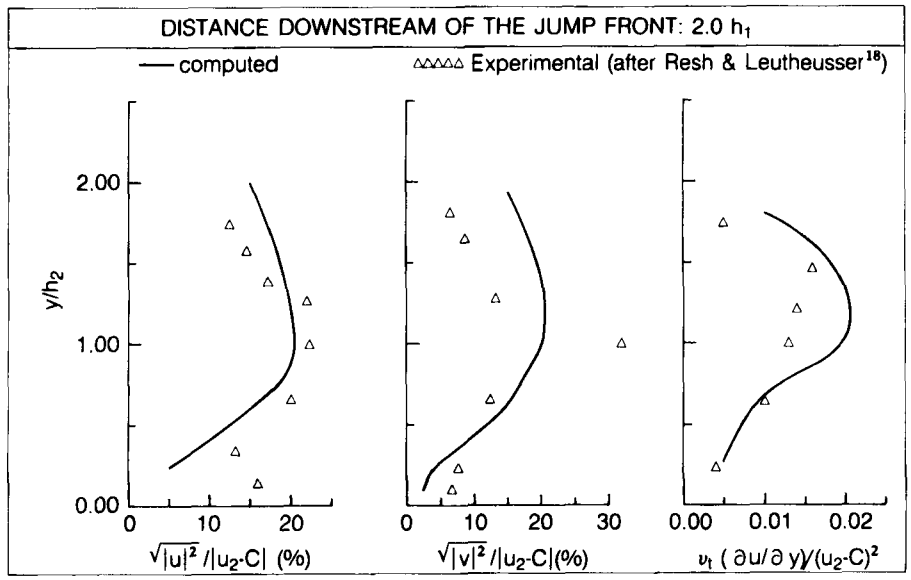

Figure 8. Computed versus experimental distributions of the dimensionless turbulent velocity fluctuations and shear stress for a hydraulic jump with $\mathbb{F} = 2{\cdot}83$

smaller than in the experiments. The computed depth ratio for this jump was within 1% of the theoretical value, again showing good overall momentum conservation. The study of the turbulent jumps provided a good verification and assessment of the predictive capabilities of the present model for strongly turbulent free surface flows.

The second numerical simulation reported here is the breaking of a solitary wave over a slope. The physical domain was chosen 12 m long and 0·5 m high and consisted of three sections (see Figure 9). The first section, from $x=0$ to 4 m, had a horizontal bottom and a still water depth of 35·5 cm. The second section, from $x=4$ to 8·3 m, had an average bottom slope of 1/20 which was defined by blocking out mesh cells. The third section, from $x=8{\cdot}3$ to 12 m, had a horizontal bottom and a still water depth of 14 cm. This set-up reproduced approximately the physical conditions of one of Nadaoka's experiments.[2] The initial and boundary conditions were as follows. A solitary wave with dimensionless height 0·25 and a crest at $x=2$ m was generated by specifying u, v, ϕ and F according to third-order solitary wave theory.[23] The initial conditions for k and ε were $k=2{\cdot}62\times10^{-3}\ \mathrm{m^2\,s^{-2}}$ and $\varepsilon=1{\cdot}07\times10^{-3}\ \mathrm{m^2\,s^{-3}}$ ($\nu_t/\nu\simeq45$). On the bottom, wall boundary conditions were imposed. The remaining boundaries were treated as open. The fluid molecular viscosity was $\nu=1{\cdot}3\times10^{-6}\ \mathrm{m^2\,s^{-1}}$ and the acceleration due to gravity was $9{\cdot}81\ \mathrm{m\,s^{-2}}$ downwards. The domain was discretized using a regular mesh of 500×50 cells. The time step was $\Delta t=2{\cdot}5\times10^{-4}$ s.

After 1 s of propagation the wave reached the slope. The wave profile was nearly symmetrical and the velocity (relative to the wave crest) was almost identical to the initial condition. The turbulent kinetic energy and the eddy viscosity were concentrated in two thin regions, one near the bottom and the other near the wave crest. In these two boundary layers k was about 1% of the kinetic energy of the mean flow and $\nu_t/\nu\simeq50$. These values were not very different from the respective initial conditions. Vorticity was concentrated in the two boundary layers, as expected. In the interior of the fluid, only residual levels were found. The turbulent shear stress was residual and spatially uncorrelated, except in the two boundary layers, where $\nu_t(\partial u/\partial y)/u^2\simeq2\times10^{-3}$. After 3 s of propagation the wave reached the last section of the domain and was at the onset of breaking. Its profile was then highly deformed, with a steep front face. The formation of a plunging jet with fluid velocities higher than the wave celerity was observed. The turbulent kinetic energy and the eddy viscosity were still concentrated in the two boundary layers. The value of k increased by 150% with respect to the pre-breaking stage but remained about 0.6% of the kinetic energy of the mean flow under the wave crest (where the plunging jet was forming). The

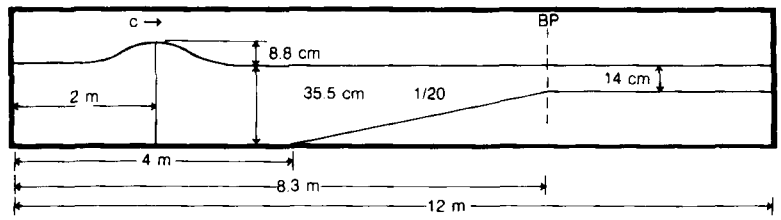

Physical parameters	Geometrical parameters		Discretization parameters
g = 9.81	length of domain	12m	I = 500 cells
$\nu = 1.3\times10^{-6}$	Height of domain	0.5m	J = 50 cells
$K_i = 2.62\times10^{-3}$	Dimensionless		$\Delta y = 1.0$ cm
$\epsilon_i = 1.07\times10^{-3}$	Wave height	0.25	$\Delta x = 2.4$ cm
$[\nu_t/\nu=45]$			$\Delta t = 2.5\times10^{-4}$ s

Figure 9. Set-up for the solitary wave problem

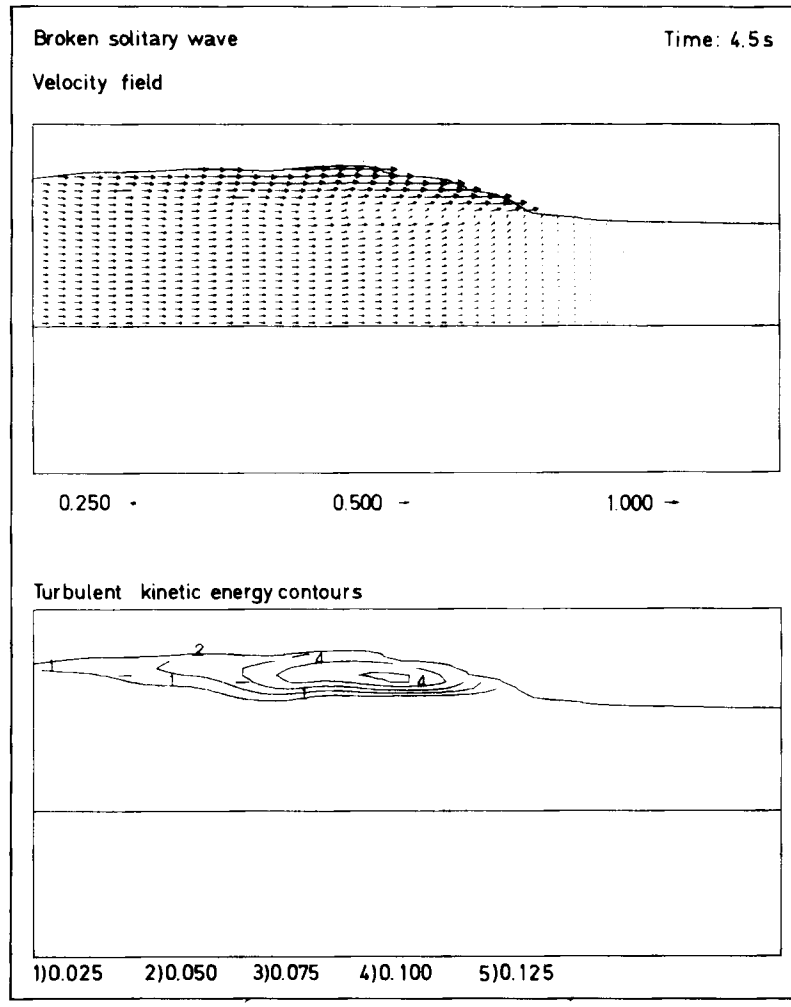

Figure 10. Velocity field (top) and turbulent kinetic energy (bottom) for the broken solitary wave after 4·5 s of propagation

turbulence Reynolds number in these boundary layers was then $\nu_t/\nu \simeq 125$ and remained close to its initial condition in the bulk of the fluid.

Figure 10 shows the mean velocity and the turbulent kinetic energy for the broken wave at $t = 4{\cdot}5$ s. A strong shear layer was formed near the surface as a consequence of the collapse of the plunging jet. The turbulence intensity in this shear layer was high ($k/(u^2+v^2) \simeq 10\%$, one order of magnitude larger than before breaking). The turbulence generated in the bottom boundary layer was irrelevant in this stage. It is observed that the downward spread of turbulence was small. Figure 11 shows the distributions of the turbulence Reynolds number ν_t/ν and the turbulent shear stress for the broken wave at the same instant. The spatial distribution of these variables was similar to that of the turbulent kinetic energy, their maxima being two orders of magnitude larger than before breaking.

The model represented the essential features of the transition from pre-breaking to broken wave motion. However, the transition was less abrupt than might be expected. The decay of the

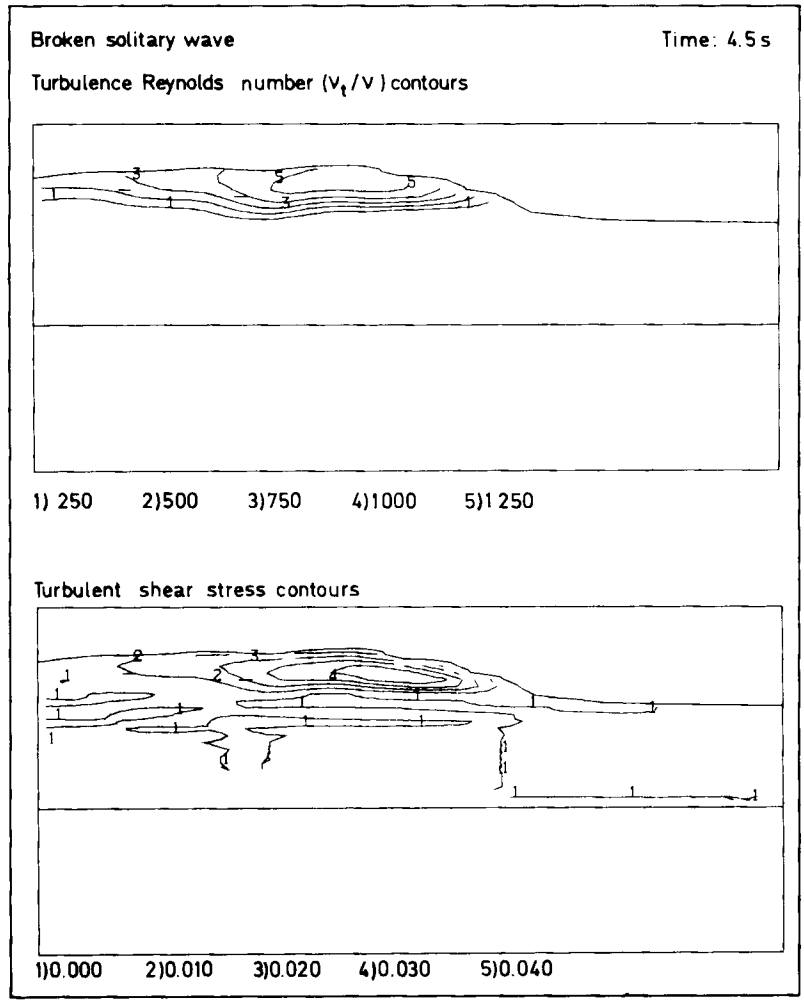

Figure 11. Turbulence Reynolds number ν_t/ν (top) and turbulent shear stress (bottom) distributions for the broken solitary wave after 4·5 s of propagation

dissipation rate ε produced too high values of the eddy viscosity before breaking started. Also, the distributions of the turbulence variables in the fully developed turbulent stage were more concentrated and had higher maxima than those found by Nadaoka[2] in experiments with periodic waves under similar physical conditions.

The last calculation reported here is the breaking of a train of periodic waves over a slope. The main purpose of this numerical experiment was to compare the dynamics of breaking periodic waves with that of the solitary waves. The physical conditions were specified as follows. The computational domain was chosen 9 m long and 0·40 m high, with a still water level of 0·30 m. Periodic waves were generated at the left boundary by means of special boundary conditions for u, v and F using second-order Stokes theory. This wave train had a height $H=6$ cm and a period $T=1{\cdot}22$ s. Starting at $x=2$ m from the left boundary, a slope of 1/20 was defined approximately by blocking out mesh cells. The waves broke over this slope as a consequence of non-linear

steepening. The acceleration due to gravity was $g = 9{\cdot}81\ \mathrm{m\,s^{-2}}$ downwards and the molecular viscosity was chosen as $\nu = 1{\cdot}3 \times 10^{-6}\ \mathrm{m^2\,s^{-1}}$. This set-up is similar to that of Mizuguchi's experiments.[24] The initial conditions for the turbulence variables were $k = 2{\cdot}253 \times 10^{-5}\ \mathrm{m^2\,s^{-2}}$ and $\varepsilon = 8{\cdot}574 \times 10^{-6}\ \mathrm{m^2\,s^{-3}}$ everywhere, corresponding to very low initial turbulence intensity. The computational domain was discretized using a regular mesh of 300×40 cells with $\Delta x = 3$ cm and $\Delta y = 1$ cm.

Figure 12 shows the mean velocity field and free surface configuration after several waves have been introduced in the computational domain. This figure also illustrates the typical sequence of transformations suffered by wind waves across a surf zone. In the initial stages of shoaling, the waves remain nearly symmetrical (waves 1 and 2). Because of non-linear steepening, the front face of the waves becomes steep; a plunging jet where the particle velocity exceeds $\sqrt{(gh)}$ is formed near the wave crest (wave 3). After breaking, the waves propagate much like moving hydraulic jumps (wave 4). Finally, a 'run-up' region is observed near the shoreline, where the mean water level is slightly higher than offshore to equilibrate the loss of wave momentum flux (or radiation stress) across the surf zone (wave 5). Figure 13 shows very clearly the fundamental difference between the velocity field of pre-breaking and broken waves. Before breaking, the velocity field remains nearly irrotational and symmetrical about the wave crest. After breaking, there is a

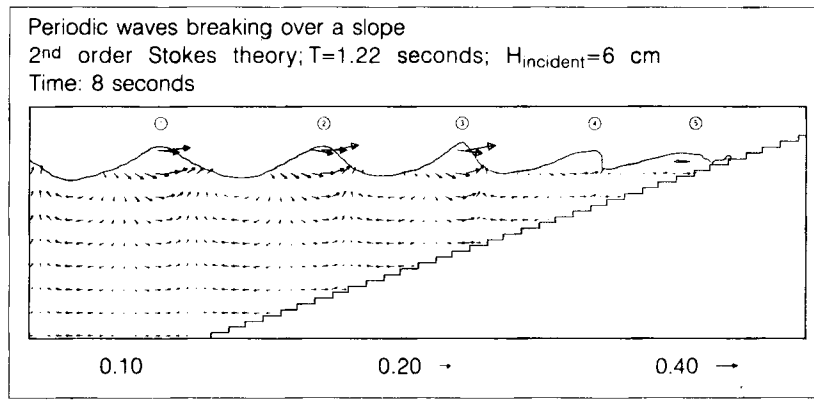

Figure 12. Mean velocity and surface configuration for a train of periodic waves at $t = 8$ s

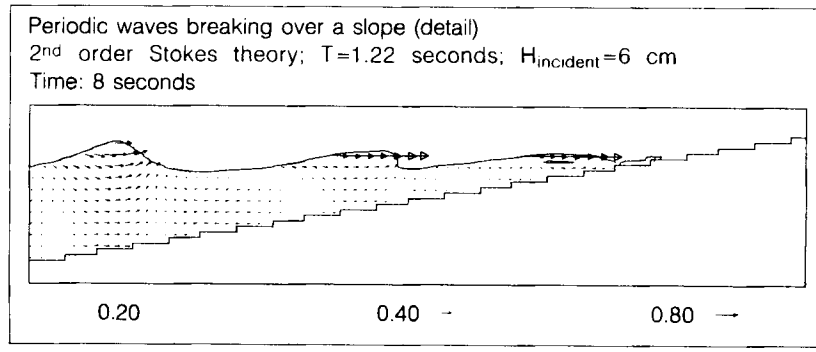

Figure 13. Detail of the velocity field in the surf zone between $x = 4{\cdot}5$ and $9{\cdot}0$ m at $t = 8$ s

strong shear layer above the trough level and vorticity is high. The rotational component of the flow is clearly responsible for most of the mass flux associated with broken waves (see also Reference 2).

Figures 14 and 15 show the contours of turbulent kinetic energy and turbulence Reynolds number ν_t/ν in the surf zone. As expected, turbulence was much more intense after breaking. The regions with high turbulence intensity were confined to the region above the trough level. As in the previous simulation, the computed distributions of the turbulence variables were more concentrated and had higher maxima than were found in experiments.[24] The computed results suggest that surf zone waves behave somewhat like a train of independent solitary waves, with a small return flow under their troughs. Most of the turbulence is dissipated where it is created. The downward spread of turbulence intensity by advective and diffusive transport is relatively slow.

Figure 16, after Mizuguchi,[24] shows experimental measurements of the velocity field (cm s^{-1}) and turbulent kinetic energy (cm^2 s^{-2}). The inclination of the small segments in the turbulent kinetic energy plot indicates the relative intensity of the velocity fluctuations. It is seen that the turbulence is nearly isotropic (approximately 45° inclination) almost everywhere.

The structure of the experimentally observed phase-averaged velocity field is very similar to that of the computed waves at approximately the same depth (wave 3). This is particularly noteworthy underneath the breaking wave crest, where remnants of the structure of the velocity

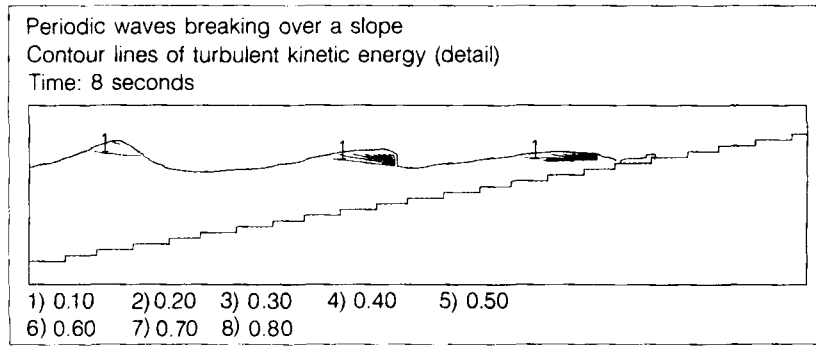

Figure 14. Contour lines of the turbulent kinetic energy in the surf zone between $x=4{\cdot}5$ and 9·0 m at $t=8$ s

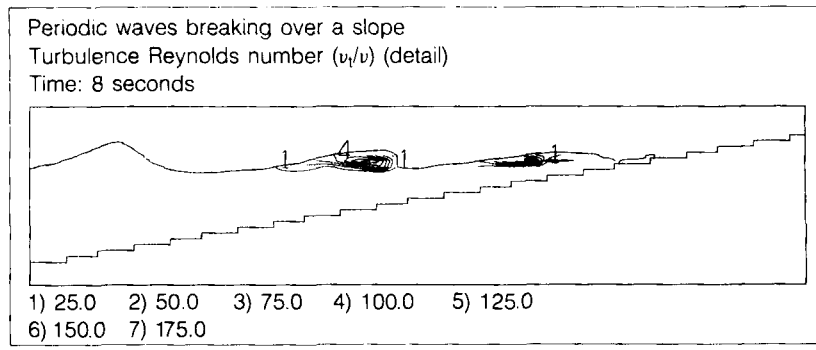

Figure 15. Contour lines of the turbulence Reynolds number ν_t/ν in the surf zone between $x=4{\cdot}5$ and 9·0 m at $t=8$ s.

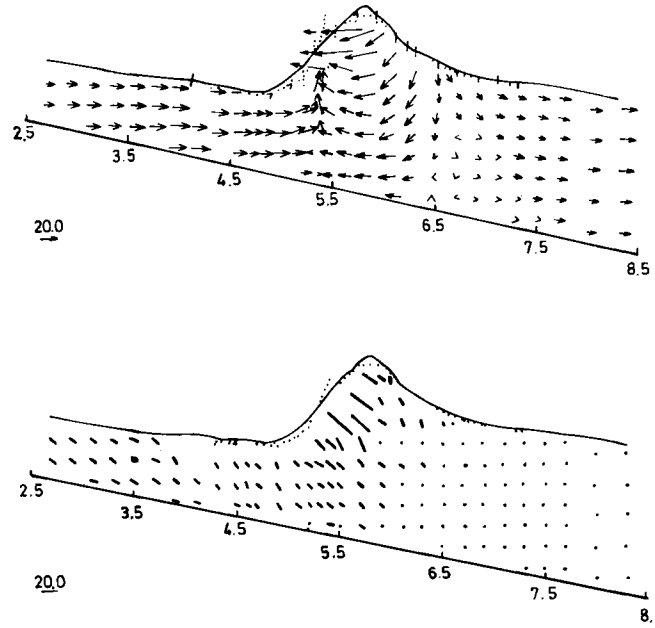

Figure 16. Experimental results of mean velocity field (top) and turbulent kinetic energy (bottom) (adapted from Mizuguchi[24])

field of the nearly irrotational overturning wave just before breaking were observed in both experimental and numerical results. Also, the magnitude of the computed velocity in the plunging jet was in fair agreement with the experimentally observed value.

The computed distribution of turbulent kinetic energy was more concentrated than the experimentally observed distribution. The regions where the computed turbulent kinetic energy was high were located above the wave trough level, whereas the experiments show significant downward spread of turbulence intensity and residual turbulence levels left by previous waves. Also, the computed maximum of turbulence was about 200% higher than the corresponding value found by Mizuguchi.

These discrepancies do not necessarily imply, however, that the k–ε model performed poorly in this test case, because the experimental investigations also have important limitations. First, in the regions where the turbulence is most intense, accurate measurements are not yet available (because of aeration). Secondly, the measurement of the Reynolds stresses in wave-breaking experiments is very sensitive to the method used for defining averages[2] and to wave–wave interaction.

Further investigation is required to fully evaluate the quality of the present model for computing turbulence properties in breaking waves, and there is much room for improvement.

7. CONCLUSIONS AND FUTURE DEVELOPMENTS

A simple, yet powerful numerical technique for transient turbulent flows involving multiple free boundaries has been presented. This technique is an extension of the SOLA-VOF algorithm[6] in which the dynamics of the turbulence is treated by introducing a especially developed k–ε model.

The present technique is capable of describing wave transformation phenomena before and after breaking and many other flow problems of practical interest. This ability was proven in several computational examples, in which the relevant properties of difficult turbulent free surface flows were predicted accurately. Thus a possible future application of the model described herein is to serve as a complement to experimental studies as a 'numerical laboratory'.

Some future developments of the model are being considered at the time of writing. A brief description of these improvements will now be outlined.

An important physical phenomenon in turbulent free surface flows is air–water mixing, which introduces non-negligible density variations and limited compressibility. Inclusion of these two effects in the present model would require an additional transport equation for the air concentration and a partial restructuring of the algorithm. Work is presently under way to incorporate these refinements.

The results reported herein indicate that the k–ε model has important limitations for representing low-intensity and non-isotropic turbulent diffusion. These limitations can be partially overcome by replacing the k–ε model by an algebraic stress or full Reynolds stress model.[3]

From the numerical viewpoint the most important spurious effect found so far is artificial roughness, which disrupts the structure of the flow near obstacles that are not aligned with the mesh. This will be eliminated in the near future by using a refinement of the pressure–velocity iteration technique which allows arbitrary cell boundaries while maintaining the same type of finite difference mesh.[8] Also, the use of more efficient discretizations for the transport equations is being considered at the time of writing.

ACKNOWLEDGEMENTS

The author is grateful to the Portuguese Navy and to the Junta Nacional de Investigação Cientifica e Tecnologica, Portugal for sponsoring this investigation. Institutional support from the Instituto Hidrografico, Portugal is also gratefully acknowledged. The author also wishes to thank Professor A. S. Arcilla and Mr. F. Collado of Catalonia University of Technology (Barcelona, Spain) for their help and interest in the present investigation, and Dr. D. A. Rodrigues for his numerous helpful and stimulating discussions.

APPENDIX: NOMENCLATURE

A	dimensionless parameter, $\ln(Eu_* y/\nu)$
C	celerity of a moving hydraulic jump
C_d, C_1, C_2	constants of k–ε turbulence model
E	constant in logarithmic law-of-the-wall
F	volume-of-fluid function
$\mathbb{F}$	Froude number
g_x, g_y	components of body force vector in co-ordinate directions x and y respectively
h_1, h_2	water levels on either side of a hydraulic jump
H	wave height
k	turbulent kinetic energy per unit mass
t	time
T	wave period
u	velocity component in x-direction
u_0	uniform velocity in grid turbulence problem
u_1, u_2	velocities on either side of a moving hydraulic jump

u_s	velocity in co-ordinate system with x-axis oriented in direction of local streamline
u_w	mean velocity at y_w
u_*	friction velocity in a constant stress boundary layer
v	velocity component in y-direction
x	horizontal co-ordinate
X	dimensionless parameter, u_*/u_w
y	vertical co-ordinate
y_w	distance from a wall
y^+	dimensionless distance, $u_* y/\nu$

Greek letters

α	parameter controlling amount of upstream differencing in approximations for advective fluxes in turbulence equations
β	constant in ν_t-damping function
γ	parameter controlling amount of upstream differencing in approximations for advective fluxes in turbulence equations
Δ	space or time increment
ε	rate of dissipation
κ	von Kármán constant
ν	kinematic molecular viscosity
ν_t	turbulent (eddy) viscosity
ρ	fluid density
$\sigma_k, \sigma_\varepsilon$	constants of k–ε model
τ_w	shear stress at a wall in a constant stress boundary layer
ϕ	pressure divided by (constant) density

REFERENCES

1. C. C. Mei, *The Applied Dynamics of Ocean Surface Waves*, Wiley–Interscience, New York, 1983.
2. K. Nadaoka, 'A fundamental study on shoaling and velocity field structure of water waves in the nearshore zone', *Tech. Rep. 36*, Deparment of Civil Engineering, Tokyo Institute of Technology, 1986.
3. W. Rodi, *Turbulence Models and Their Application in Hydraulics*, IAHR, Delft, 1980.
4. B. E. Launder and D. B. Spalding, *Lectures in Mathematical Models of Turbulence*, Academic, London, 1972.
5. B. D. Nichols and C. W. Hirt, 'Methods for calculating multi-dimensional, transient free-surface flows past bodies', *Proc. 1st Int. Conf. on Numerical Ship Hydrodynamics*, Gaithersburg, MD, October 1975.
6. B. D. Nichols, C. W. Hirt and R. S. Hotchkiss, 'SOLA-VOF: a solution algorithm for transient fluid flow with multiple free-boundaries', *Los Alamos Scientific Laboratory Rep. LA-8355*, 1980.
7. A. C. Hindmarsh, P. M. Gresho and D. F. Griffiths, 'The stability of explicit Euler time-integration for certain finite-difference approximations of the multi-dimensional advection–diffusion equation', *Int. j. numer. methods fluids*, **4**, 853–897 (1984).
8. C. W. Hirt, B. D. Nichols and N. C. Romero, 'SOLA: a solution algorithm for transient fluid flows', *Los Alamos Scientific Laboratory Rep. LA-5852*, 1975.
9. W. P. Jones and B. E. Launder, 'The prediction of laminarization with a 2-equation model of turbulence', *Int. J. Heat Mass Transfer*, **15**, 301–314 (1972).
10. F. H. Harlow and P. I. Nakayama, 'Turbulence transport equations', *Phys. Fluids*, **11**, 2323–2332 (1967).
11. F. H. Harlow and P. I. Nakayama, 'Transport of turbulence energy decay rate', *Los Alamos Scientific Laboratory Rep. LA-3854*, 1968.
12. J. O. Hinze, *Turbulence*, 2nd edn, McGraw-Hill Classic Textbook Reissue Series, New York, 1975.
13. J. K. Dukowicz and J. D. Ramshaw, 'Tensor viscosity method for convection in numerical fluid dynamics', *J. Comput. Phys.*, **32**, 71–79 (1979).
14. A. A. Amsden and F. H. Harlow, 'The SMAC method: a numerical technique for calculating incompressible fluid flows', *Los Alamos Scientific Laboratory Rep. LA-4370*, 1970.
15. P. M. Gresho and R. L. Sani, 'On pressure boundary conditions for the incompressible Navier–Stokes equations', *Int. j. numer. methods fluids*, **7**, 1111–1145 (1987).

16. H. H. Fernholz, 'External flows', in P. Bradshaw (ed.), *Turbulence*, Springer, Heidelberg, 1978.
17. B. E. Launder, 'Second-moment closure and its use in modelling turbulent industrial flows', *Int. j. numer methods fluids*, **9**, 963–985 (1989).
18. F. J. Resh and H. J. Leutheusser, 'Reynolds stress measurements in hydraulic jumps', *J. Hydraul. Res.*, **10**, 40–430 (1972).
19. J. A. Battjes, 'Surf-zone dynamics', *Ann. Rev. Fluid Mech.*, **20**, 257–293 (1988).
20. P. A. Madsen and I. A. Svendsen, 'Turbulent bores and hydraulic jumps', *J. Fluid Mech.*, **129**, 1–25 (1983).
21. I. A. Svendsen and P. A. Madsen, 'A turbulent bore on a beach', *J. Fluid Mech.*, **148**, 73–96 (1984).
22. I. A. Svendsen, 'Analysis of surf-zone turbulence', *J. Geophys. Res.*, **92**, 5115–5124 (1987).
23. J. D. Fenton, 'A ninth order solution for the solitary wave', *J. Fluid Mech.*, **53**, 257–271 (1972).
24. M. Mizuguchi, 'Experimental study on kinematics and dynamics of wave breaking', *Proc. Int. Conf. on Coastal Engineering*, ASCE, New York, 1986, pp. 589–603.